Indian Journal of Chemistry
Vol. 65, May 2026, pp. 475-492
DOI: 10.56042/ijc.v65i5.25708

Unveiling mechanism of action of alkaloids from *Macleaya microcarpa* as NF-κB inhibitors for gastric cancer: Insights from network pharmacology, molecular docking, dynamics simulations and ADMET prediction

Lan Thi Ngoc Nguyen, Tan Quang Tu, Hung Duc Nguyen* & Mau Hoang Chu
Thai Nguyen University of Education, 24000, Thai Nguyen, Vietnam
E-mail: hungnd@tnue.edu.vn

Received 20 November 2025; accepted (revised) 14 May 2026

Gastric cancer, a highly aggressive malignancy, ranks fifth globally in new cases and deaths in 2022. Natural products from traditional Chinese medicine exhibit potential in cancer therapy. The present study investigates the mechanism of benzophenanthridine alkaloids from *Macleaya microcarpa* as potential anti-gastric cancer agents, targeting the NF-κB-inducing kinase (NIK, protein ID: 4G3F). The results indicate that CPD1 likely modulates the non-canonical NF-κB pathway, with molecular docking revealing a superior binding energy (–9.86 kcal/mol) compared to IMD 0354 (–7.61 kcal/mol). Molecular dynamics simulations over 100 ns confirm stable interactions, with RMSD ranging from 0.20 to 0.25 nm, Rg around 2.1 nm, and SASA from 150 to 165 nm², supporting a robust binding profile. *In silico* ADMET analysis demonstrates high intestinal absorption, limited distribution, CYP3A4 metabolism, and a good clearance rate, with no AMES toxicity. These results position CPD1 as a promising NIK inhibitor for gastric cancer therapy.

Keywords: ADMET, Alkaloid, Gastric cancer, *Macleaya microcarpa*, Molecular modeling, Nuclear factor kappa B

Gastric cancer is a highly aggressive and heterogeneous cancer. In 2022, gastric cancer was ranked as the fifth most common cancer in terms of both new cases and deaths globally. While incidence and mortality rates have decreased in some regions due to improved healthcare and living conditions, gastric cancer remains a significant public health concern, particularly in low- and middle-income countries[1]. Although surgery is a primary treatment for gastric cancer, the timing of surgery is not solely determined by chemotherapy susceptibility. While chemotherapy can be used before or after surgery to improve outcomes, the optimal timing is based on the stage and resectability of the tumor, as well as the patient's overall condition[2].

Traditional Chinese medicine has indeed been utilized for thousands of years to prevent and treat diseases. It offers several potential advantages in cancer treatment by inhibiting cancer cell proliferation, migration, induce apoptosis, and affect angiogenesis. These include symptom management, improved quality of life, and potentially enhanced immune function and reduced side effects from conventional therapies[3]. Research into the active components of traditional Chinese medicine is gaining traction due to their potential as lead compounds for drug development and their role in traditional medicine formulations[4]. These active ingredients, found in various herbs and natural substances, can be isolated and studied for their therapeutic properties, potentially leading to new drugs and a deeper understanding of mechanisms[5]. Traditional Chinese medicines exhibit biological activity attributed to bioactive constituents, notably alkaloids. These compounds demonstrate substantial potential in cancer therapy due to their capacity to disrupt critical cellular processes associated with tumor proliferation and persistence. They can suppress cell division, initiate apoptosis, and regulate signaling pathways essential for cancer advancement[6]. Among these pathways, the Nuclear Factor kappa B (NF-κB) signaling pathway, particularly its non-canonical branch regulated by the NF-κB-inducing kinase (NIK), is a crucial regulator of gastric cancer cell survival and inflammation. It plays a significant role in the development and progression of gastric cancer by influencing cell proliferation, apoptosis, and inflammation[7]. Thus, modulating this pathway through targeting NIK represents a promising therapeutic strategy for diseases like cancer and inflammatory conditions. Consequently, alkaloids are highly promising candidates for lung cancer treatment,

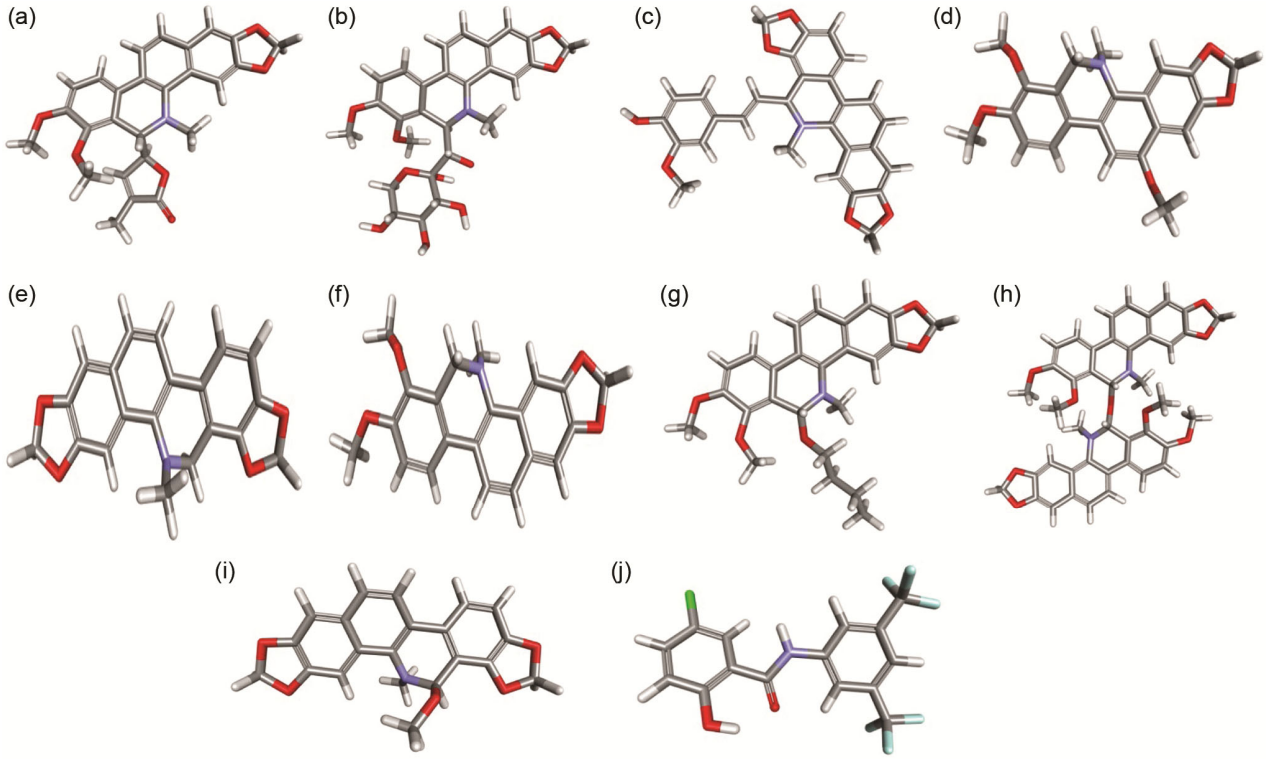

Fig. 1 — 3D structure of the selected alkaloidss. (A) CPD1, (B) CPD2, (C) CPD3, (D) CPD4, (E) CPD5, (F) CPD6, (G) CPD7, (H) CPD8, (I) CPD9 and (J) the comparative reference, IMD 0354

given their ability to induce programmed cell death, or apoptosis, in cancerous cells. In traditional Chinese medicine, *Macleaya microcarpa* is primarily used for treating skin diseases and inflammation, as well as for its insecticidal and anthelmintic properties. According to contemporary pharmacological research, this species contains benzophenanthridine alkaloids possessing potential cytotoxicity properties against gastric cancer cell-line (BGC-823)[8]. However, the mechanism at molecular level of its cytotoxicity properties and type of action remain unexplore. Therefore, this study aimed to discover and evaluate the mechanism of benzophenanthridine alkaloids isolated from *M. microcarpa* using network pharmacology and molecular modeling approach. The findings provide a foundation for future experimental validation and optimization of benzophenanthridine alkaloids as effective and safe treatments for gastric cancer, pending further *in vitro* and *in vivo* studies.

Experimental Section

Collection and preparation of ligands

The benzophenanthridine alkaloids from *M. microcarpa* possessing cytotoxic activity against human gastric cancer (BGC-823) were collected through literature source[8]. For details, these selected alkaloids, including maclekarpine A (CPD1), maclekarpine D (CPD2), maclekarpine E (CPD3), 6-methoxy dihydrochelerythrine (CPD4), dihydros anguinarine (CPD5), dihydrochelerythrine (CPD6), 6-butoxy dihydrochelerythrine (CPD7), bis[6-(5,6-dihydrochelerythrinyl)]ether (CPD8), 6-methoxy dihydrosanguinarine (CPD9), have molecular formulas of $C_{26}H_{23}NO_6$, $C_{27}H_{29}NO_{10}$, $C_{29}H_{23}NO_6$, $C_{22}H_{21}NO_5$, $C_{20}H_{15}NO_4$, $C_{21}H_{19}NO_4$, $C_{25}H_{27}NO_5$, $C_{24}H_{36}N_2O_9$, $C_{21}H_{17}NO_5$, and molecular weights of 445.1525, 527.1791, 481.1525, 379.1420, 333.1001, 349.1314, 421.1889, 712.2421, 363.1107 *m/z*, respectively (Fig. 1). The 2D structures of ligands were prepared in .sdf format using ChemDraw Prime v23.1 (Perkin Elmer, USA) and converted to 3D structures in .pdb format using Biovia Discovery Studio Visualizer v24.1 (DassaultSystemes BIOVIA, USA). Polar hydrogens and Gasteiger charges were also added, and all torsion angles were allowed to rotate using AutoDock Tools 1.5.7 (Center for Computational Structural Biology, USA). The 2D structure of the comparative reference, IMD 0354 (PubChem CID: 5081913) possessing molecular formula of $C_{15}H_8ClF_6NO_2$ and molecular weight of

383.0148 *m/z*, was obtained from the PubChem database in .sdf format (https://pubchem.ncbi.nlm.nih.gov) and further converted to .pdb format using Biovia Discovery Studio Visualizer.

Molecular target prediction

The 2D structural similarity between each drug and the ligand set of each target was quantified as an expectation value (E-value) using the Similarity Ensemble Approach (SEA)[9]. The SMILES strings for the selected alkaloids were obtained and entered into the SEA database (http://sea.bkslab.org), with *Homo sapiens* specified as the target organism to ensure predictions relevant to human biology. This approach facilitated the identification of biological processes potentially affected by these alkaloids, providing a foundation for further investigation into their mechanisms of action.

Protein-protein interaction network prediction

The protein-protein interaction (PPI) networks for the selected alkaloids were examined using the STRING database (https://string-db.org)[10]. Potential target proteins identified *via* SEA analysis were entered into STRING, with *Homo sapiens* specified as the reference organism to ensure human biological relevance. These networks are essential for understanding the compounds' potential mechanisms of action from a systems biology viewpoint.

Biosignaling network prediction

The X2K Web platform (https://maayanlab.cloud/X2K/) was employed to explore upstream regulatory networks of alkaloids target proteins, combining predictive insights with molecular pathway analysis[11]. X2K synthesizes transcription factor, kinase, and protein-protein interaction data to build regulatory networks for gene sets obtained from SEA and STRING, with *Homo sapiens* designated as the reference species.

Molecular docking

The 3D structures of all selected alkaloids were generated in .pdb format using Biovia Discovery Studio Visualizer, with only polar hydrogens and Compute Gasteiger charges added, and all torsions permitted to rotate[12]. The 3D conformation of the target NF-κB-inducing kinase (NIK) (protein ID: 4G3F) was obtained in .pdb format from the RCSB Protein Data Bank (https://www.rcsb.org/)[13]. The structural quality of protein 4G3F was assessed by examining the phi (φ) and psi (ψ) torsion angles using a Ramachandran plot generated by PROCHECK (Program to Check the Stereochemical Quality of Protein Structures)[14]. Molecular docking of the protein and ligands was conducted using AutoDock Tools. The grid was configured with dimensions x = 62, y = 50, z = 50, and a grid point spacing of 0.375 Å. The docking site coordinates were set at x = 15.579 Å, y = 12.456 Å, and z = 3.775 Å within the 4G3F protein binding pocket. The Lamarckian genetic algorithm was employed to identify the most energetically favorable ligand-protein binding conformations.

Molecular dynamics simulation

Molecular dynamics simulations for the best-docked conformation with the 4G3F protein were performed over 100 ns using GROMACS v2024.4[15]. The protein structure was refined using Swiss-PdbViewer to correct for missing atoms and residues[16]. Ligand topologies were created with SwissParam[17]. The solvation system employed a triclinic simulation box customized for the protein-ligand complex, utilizing the SPC water model, with a 0.15 M sodium chloride solution added. Structural optimization and neutralization involved 50,000 steps of energy minimization. Equilibration was achieved *via* a 200 ps NVT simulation (constant number of atoms, volume, and temperature), followed by a 200 ps NPT simulation (constant number of atoms, pressure, and temperature), stabilizing the system at 300 K and 1.0 bar. Three 100-nanosecond simulations were conducted per system with a 2-femtosecond (0.002 ps) time step, and trajectory data were saved every 10 ns. Simulation data were analyzed using Grace software (Grace Development Team) to assess parameters such as root mean square deviation (RMSD), root mean square fluctuation (RMSF) of residues, radius of gyration (Rg), number of hydrogen bonds (H-bonds), and solvent-accessible surface area (SASA). The conformational stability of docked compounds was evaluated through superimposition using UCSF Chimera 1.19[18]. Ligand structures at 0 ns and 100 ns were aligned to the protein's binding pocket to examine the persistence of interactions with key amino acid residues, including hydrogen bonds, Van der Waals forces, and hydrophobic interactions, over the simulation period. This analysis provided insights into the dynamic behavior and binding stability of the

ligand-protein interactions throughout the 100 ns duration.

In silico pharmacokinetics ADMET prediction

Evaluating the ADMET properties (Absorption, Distribution, Metabolism, Excretion, and Toxicity) is indeed a critical step in lead optimization during drug discovery. This evaluation helps determine how well a potential drug candidate interacts with the body, its effectiveness, and potential safety concerns. Thus, an ADMET study was conducted using the pkCSM online server to evaluate the pharmacokinetic and toxicity properties of selected alkaloids[19].

Results and Discussion

Protein structure preparation and validation

A Ramachandran plot was constructed utilizing the PROCHECK software to evaluate the stereochemical quality of the refined 4G3F protein structure, which corresponds to the NIK, a key regulator within the non-canonical NF-κB signaling pathway implicated in the proliferation and survival of gastric cancer cells. This plot delineates the conformational space into distinct regions based on the distribution of Φ and Ψ dihedral angles, reflecting the energetically favorable orientations of amino acid residues derived from a database of high-resolution protein structures. The Φ angles are plotted along the x-axis, while the Ψ angles are represented along the y-axis, indicating residue conformations. For the 4G3F structure, the analysis revealed that 91.8% of residues, excluding glycine and proline, reside within the most favored regions (A, B, L) with a count of 236 residues, 7.0% are situated in the additionally allowed regions (a, b, l, p) with a count of 18 residues, 0.8% are located in the generously allowed regions (~a, ~b, ~l, ~p) with a count of 2 residues, and 0.4% are present in disallowed regions with a count of 1 residue, based on a total of 257 assessed non-glycine and non-proline residues, representing 100.0% of this subset. The overall structure comprises a total of 312 residues, including 4 end-residues (excluding glycine and proline), 30 glycine residues, and 21 proline residues (Fig. 2).

This distribution aligns with the criteria for a high-quality structural model, where a minimum of 90% of residues are expected in the most favored regions, derived from an analysis of 118 structures with a resolution of at least 2.0 Å and an R-factor not exceeding 20%. The minimal presence of residues in

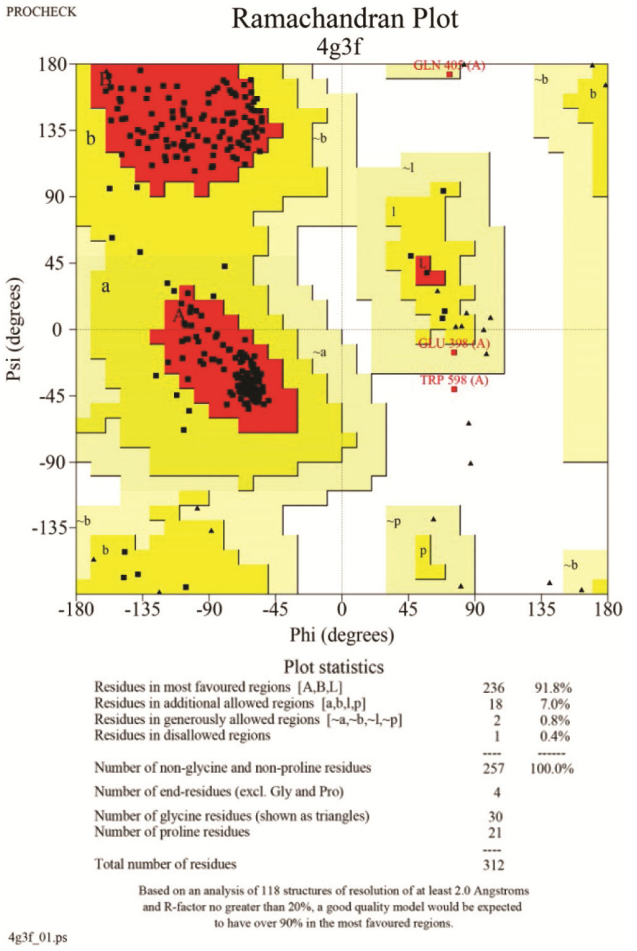

Fig. 2 — Ramachandran plot of energy-minimized predicted structures of 4G3F for NF-κB inhibition studies

disallowed regions (0.4%) supports the structural reliability of 4G3F, establishing it as a suitable template for molecular docking and simulation studies. This structural robustness enhances the accuracy of predicting interactions between alkaloids from *M. microcarpa* and the NIK binding site, thereby facilitating the assessment of their potential to inhibit the non-canonical NF-κB pathway and their efficacy as anticancer agents targeting gastric cancer cells.

Molecular target, protein interaction, and biosignaling network

Based on the molecular target predictions detailed in Table 1, the identified alkaloids exhibit associations with several significant human targets, encompassing Ras-related C3 botulinum toxin substrate 1 (RAC1), DNA topoisomerase 2-beta (TOP2B), Cytochrome P450 1A1 (CYP1A1), Solute carrier family 22 member 2 (SLC22A2), Nuclear receptor subfamily

Table 1 — Molecular target prediction of selected alkaloids

S.No.	Target gene	Description	P-value	MaxTC
CPD1	RAC1	Ras-related C3 botulinum toxin substrate 1	7.59E-13	0.38
	TOP2B	DNA topoisomerase 2-beta	9.08E-09	0.33
	CYP1A1	Cytochrome P450 1A1	2.02E-07	0.66
	SLC22A2	Solute carrier family 22 member 2	2.31E-06	0.37
CPD2	RAC1	Ras-related C3 botulinum toxin substrate 1	3.25E-13	0.39
	NR0B1	Nuclear receptor subfamily 0 group B member 1	6.21E-09	0.32
	TOP2B	DNA topoisomerase 2-beta	1.12E-08	0.33
	CYP1A1	Cytochrome P450 1A1	1.13E-06	0.59
CPD3	CXCL12	Stromal cell-derived factor 1	1.74E-75	0.33
	RAC1	Ras-related C3 botulinum toxin substrate 1	1.60E-20	0.31
	MAPT	Microtubule-associated protein tau	1.66E-20	0.44
	RGS17	Regulator of G-protein signaling 17	1.51E-19	0.31
	ODC1	Ornithine decarboxylase	5.55E-16	0.33
	NFKB1	Nuclear factor NF-kappa-B p105 subunit	1.34E-14	0.32
	GLO1	Lactoylglutathione lyase	1.26E-12	0.32
	APP	Amyloid-beta precursor protein	1.34E-12	0.44
	IKBKG	NF-kappa-B essential modulator	8.78E-12	0.32
	NFE2L2	Nuclear factor erythroid 2-related factor 2	7.76E-09	0.38
	TOP2B	DNA topoisomerase 2-beta	1.78E-08	0.32
	EP300	Histone acetyltransferase p300	2.97E-06	0.32
	CYP1A1	Cytochrome P450 1A1	6.49E-06	0.51
CPD4	RAC1	Ras-related C3 botulinum toxin substrate 1	6.08E-13	0.38
	DRD1	D(1A) dopamine receptor	7.79E-08	0.42
	DRD5	D(1B) dopamine receptor	8.88E-08	0.42
	HTR2B	5-hydroxytryptamine receptor 2B	2.05E-06	0.38
CPD5	RGS17	Regulator of G-protein signaling 17	5.86E-27	0.43
	RAC1	Ras-related C3 botulinum toxin substrate 1	2.03E-24	0.43
	NR0B1	Nuclear receptor subfamily 0 group B member 1	2.29E-08	0.3
	CYP1A1	Cytochrome P450 1A1	3.65E-08	0.44
CPD6	RAC1	Ras-related C3 botulinum toxin substrate 1	1.12E-25	0.47
	RGS17	Regulator of G-protein signaling 17	1.38E-19	0.31
	F3	Tissue factor	5.23E-11	0.34
	TOP2B	DNA topoisomerase 2-beta	1.78E-09	0.36
	CYP1A1	Cytochrome P450 1A1	5.59E-07	0.62
	DRD5	D(1B) dopamine receptor	1.72E-06	0.41
	DRD1	D(1A) dopamine receptor	9.80E-06	0.41
CPD7	RAC1	Ras-related C3 botulinum toxin substrate 1	2.23E-13	0.4
	FSHR	Follicle-stimulating hormone receptor	4.39E-13	0.3
	TOP2B	DNA topoisomerase 2-beta	1.61E-09	0.36
	CYP1A1	Cytochrome P450 1A1	2.24E-08	0.75
	F3	Tissue factor	8.08E-08	0.34
	EDNRA	Endothelin-1 receptor	3.86E-07	0.32
	EDNRB	Endothelin receptor type B	3.96E-07	0.32
	HTR2B	5-hydroxytryptamine receptor 2B	4.72E-06	0.39
	RAC1	Ras-related C3 botulinum toxin substrate 1	1.83E-24	0.45
	RGS17	Regulator of G-protein signaling 17	1.04E-18	0.3
	TOP2B	DNA topoisomerase 2-beta	4.61E-10	0.38
	CYP1A1	Cytochrome P450 1A1	1.23E-09	0.88
	F3	Tissue factor	6.73E-08	0.34
	EDNRB	Endothelin receptor type B	8.87E-07	0.34
	SLC22A2	Solute carrier family 22 member 2	4.56E-06	0.35
	HTR2B	5-hydroxytryptamine receptor 2B	9.79E-06	0.35
CPD9	RGS17	Regulator of G-protein signaling 17	1.05E-24	0.4
	RAC1	Ras-related C3 botulinum toxin substrate 1	9.23E-24	0.4
	CYP1A1	Cytochrome P450 1A1	4.15E-11	0.73
	TOP2B	DNA topoisomerase 2-beta	7.17E-09	0.33

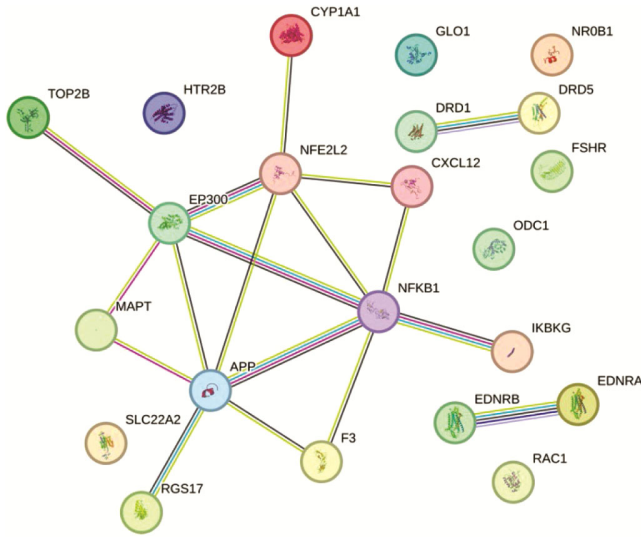

Fig. 3 — Protein-protein interactions of molecular targets of selected alkaloids

0 group B member 1 (NR0B1), Stromal cell-derived factor 1 (CXCL12), Microtubule-associated protein tau (MAPT), Regulator of G-protein signaling 17 (RGS17), Ornithine decarboxylase (ODC1), Nuclear factor NF-κB p105 subunit (NFKB1), Lactoylglutathione lyase (GLO1), Amyloid-beta precursor protein (APP), NF-κB essential modulator (IKBKG), Nuclear factor erythroid 2-related factor 2 (NFE2L2), Histone acetyltransferase p300 (EP300), D(1A) dopamine receptor (DRD1), D(1B) dopamine receptor (DRD5), 5-hydroxytryptamine receptor 2B (HTR2B), Tissue factor (F3), Follicle-stimulating hormone receptor (FSHR), Endothelin-1 receptor (EDNRA), and Endothelin receptor type B (EDNRB), among additional candidates. Of particular note, NFKB1 (NF-κB p105 subunit) represents a critical protein engaged in cellular signaling processes, predominantly within the NF-κB signaling cascade, whereas targets such as TOP2B and CYP1A1 suggest potential roles in DNA replication and xenobiotic metabolism relevant to cancer biology. Within the framework of the present investigation, which focuses on suppressing cancer signaling through the NF-κB pathway in gastric cancer, NIK does not appear directly in the SEA dataset but emerges as a promising target based on complementary analyses conducted using STRING and X2K. This finding emphasizes the involvement of NIK in modulating the survival and proliferation of gastric cancer cells, establishing it as a significant focus for subsequent exploration through molecular docking and network-based methodologies.

The protein-protein interaction network, generated through the STRING database, exhibited a comprehensive framework of interactions among the predicted molecular targets, with NFE2L2, NFKB1, APP, and EP300 identified as central nodes owing to their extensive connectivity (Fig. 3). This observation indicates that these proteins likely serve as pivotal mediators in regulating cellular responses to selected alkaloids, especially in inhibiting survival and proliferation signaling within gastric cancer cells.

Subsequent analysis employing the STRING network, centered on NFKB1, demonstrated direct interactions with proteins including IKBKG, EP300, and CXCL12, as illustrated in Fig. 3. These interactions underscore NFKB1's central role in modulating the NF-κB signaling pathway, with IKBKG facilitating pathway activation through the IKK complex and EP300 enhancing transcriptional regulation of NF-κB target genes. CXCL12 contributes to NF-κB activation within the tumor microenvironment, amplifying inflammatory and survival signaling in gastric cancer cells. The presence of IKBKG highlights a mechanism involving NF-κB pathway induction, potentially influencing the expression of pro-inflammatory and anti-apoptotic genes.

Further examination revealed interactions involving APP (Amyloid-beta precursor protein), NFE2L2 (Nuclear factor erythroid 2-related factor 2), and CYP1A1 (Cytochrome P450 1A1), extending the network's relevance to NF-κB regulation. APP may participate in signaling cascades that intersect with NF-κB activity, potentially modulating its downstream effects. NFE2L2, a regulator of oxidative stress responses, likely influences NF-κB activation under oxidative conditions, a process relevant to gastric cancer progression. CYP1A1, involved in xenobiotic metabolism, suggests a role in processing on selected alkaloids possibly altering their efficacy in targeting the NF-κB pathway. For compounds interacting with additional proteins such as TOP2B (DNA topoisomerase 2-beta) and RGS17 (Regulator of G-protein signaling 17), roles in DNA replication (TOP2B) and G-protein signaling (RGS17) may indirectly support NF-κB modulation by affecting cellular homeostasis and signaling networks.

The NIK, represented by the 4G3F structure, emerges as a critical upstream regulator not explicitly included in the SEA dataset but identified through STRING and X2K analyses. NIK's activation of the

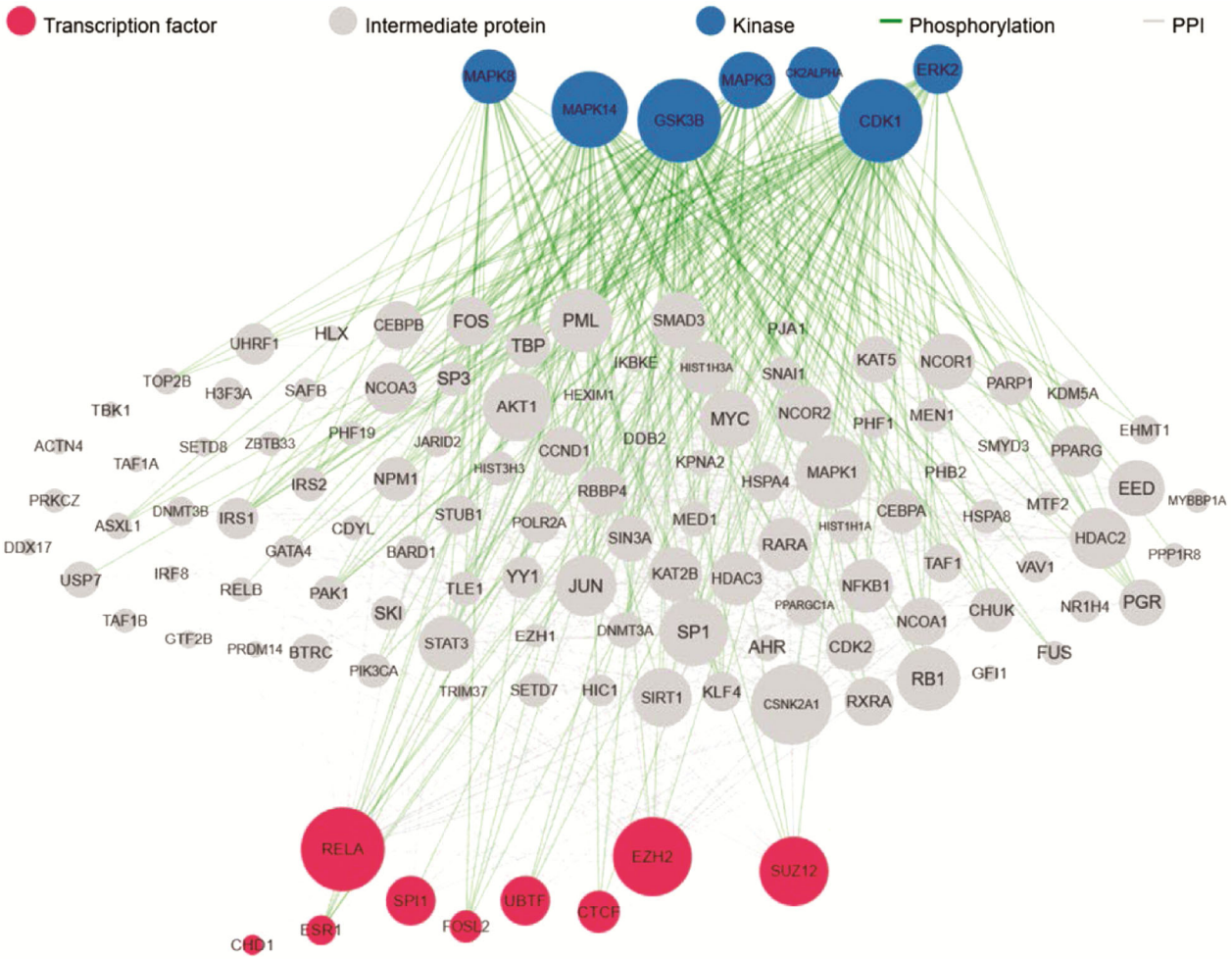

Fig. 4 — Network of kinases and transcription factors linked to molecular targets of selected alkaloids

non-canonical NF-κB pathway, facilitated by phosphorylation of IKKα and subsequent processing of p100 into p52, underscores its importance in maintaining NF-κB signaling in gastric cancer cells. This role is enhanced by additional kinases, including MAPK8 and ERK2, identified within the X2K network, which may contribute to NF-κB modulation through stress-related signaling cascades. Transcription factors such as RELA and EZH2, also highlighted in the X2K analysis, regulate gene expression associated with NF-κB activity, further reinforcing NIK's significance as a primary target for molecular docking studies with the investigated alkaloids (Fig. 4).

The pharmacological mechanism of the identified alkaloids has been elucidated through molecular target predictions, protein-protein interaction network analysis, and biosignaling pathway assessment, providing a basis for their integration into docking studies targeting NIK (4G3F). The analysis identified IKBKB, an upstream regulatory kinase, as a critical factor in sustaining NF-κB signaling, directly supporting the docking of alkaloids into the 4G3F protein to suppress NIK activity (Fig. 5A). MAPK1 and MAPK8, recognized as central nodes within the PPI network, participate in signaling cascades associated with inflammatory responses and stress-related pathways, contributing to cellular conditions that enhance NF-κB pathway modulation, a mechanism corroborated by docking analyses. CXCL12, highlighted in the molecular target predictions, may engage in microenvironmental signaling, potentially augmenting NIK inhibition through supplementary regulatory pathways, consistent with the docking strategy targeting NIK[20,21]. NIK, a kinase associated with survival signaling within the biosignaling network, is likely inhibited under these conditions, facilitating of the

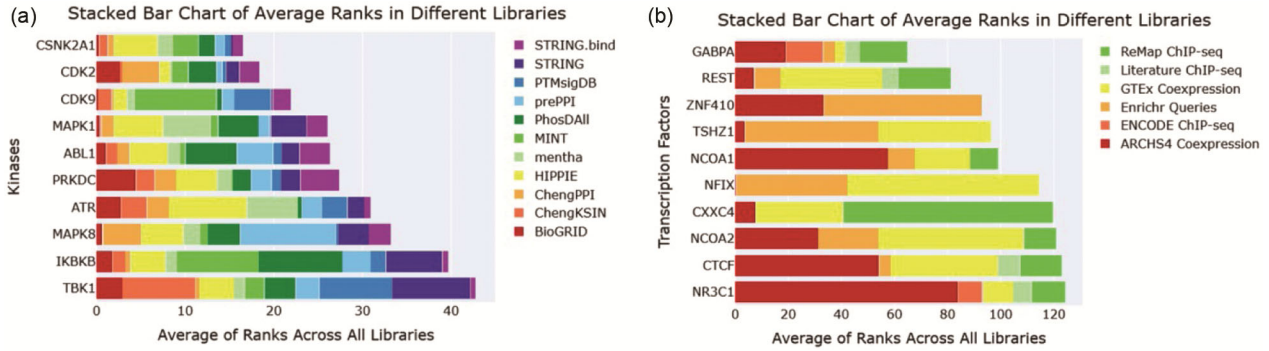

Fig. 5 — Selected alkaloids associated with kinases (A) and transcription factors (B) average rank across biological libraries

non-canonical NF-κB pathway[22]. Transcription factors such as RELA and CTCF, identified through X2K analysis, regulate the expression of genes involved in inflammatory and epigenetic responses, reinforcing the NF-κB signaling modulation pathway targeted by the docking approach (Fig. 5B). Additionally, CYP1A1, a significant protein in the PPI network and a marker of xenobiotic metabolism in cancer cells, suggests that alkaloids may modulate metabolic activity, thereby increasing intracellular compound concentrations and enhancing NIK inhibitory signaling, a proposition supported by docking into 4G3F. Other kinases, including CSNK2A1, CDK2, CDK9, ABL1, PRKDC, ATR, and TBK1, and transcription factors such as GABPA, REST, ZNF410, TSHZ1, NCOA1, NFIX, CXXC4, NCOA2, and NR3C1, identified in the X2K network, may contribute to the broader regulation of NF-κB signaling and cellular responses, further supporting the potential efficacy of the alkaloids in targeting gastric cancer cells.

These observations align with prior investigations into the modulation of survival signaling by natural compounds in cancer cells, where cellular stress and transcription factor regulation emerge as critical determinants influencing NF-κB pathway activity[23,24]. The identification of TOP2B as a potential target from molecular target predictions supports the ability of selected alkaloids to induce DNA damage, a potential upstream mechanism contributing to NIK inhibition in gastric cancer cells[25], a process further examined through molecular docking. However, the involvement of NFKB1, detected within the biosignaling network and recognized for its intricate regulatory role in cellular responses, suggests a complex regulatory framework necessitating additional exploration to clarify its influence on BGC-823 resistance. The synthesis of molecular target predictions, protein-protein interaction profiling, and biosignaling network analysis has thus established a solid foundation for selecting 4G3F as the primary docking target, offering a comprehensive understanding of the therapeutic potential of these alkaloids in suppressing cancer signaling *via* NIK in gastric cancer cells, with a potential secondary effect of modulating cell viability.

Molecular docking analysis

Molecular docking is a computational technique used in structure-based drug design to predict how small molecules bind to larger target molecules. It helps in understanding and predicting the binding affinity and mode of interaction between the ligand and the target, which is crucial for drug discovery. This study evaluated the binding energy and interactions between the protein 4G3F and the selected alkaloids compared to IMD 0354. Visualization of the 4G3F protein structure revealed the active sites, including Val408, Gly411, Val416, Ala429, Val430, Lys431, Glu442, Ile469, Met471, Leu473, Leu474, Asp521, Asn522, Leu524, And Asp536 (Fig. 6A). Before performing docking analysis, it is essential to perform redocking of the protein 4G3F to validate the docking protocol. The redocking process involved the co-crystallized ligand, and its execution yielded results presented in Fig. 6B. The reliability of the docking protocol was established through an RMSD value of 1.2696 Å, accompanied by the superposition of the original and docked ligands, confirming the accuracy of the procedure. An RMSD value below 2 Å is generally accepted as indicative of a robust docking methodology[26].

The interactions of the selected alkaloids within the binding pockets of the protein 4G3F are presented in Table 2. The amino acid residues engaged in these interactions, along with their precise locations within

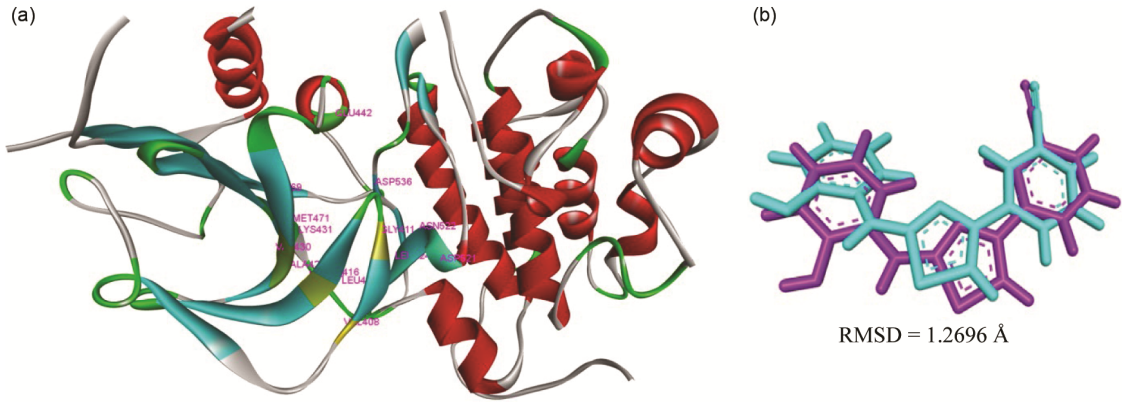

Fig. 6 — The active sites in the 4G3F protein (A) and the superposition of the docked and original ligands validating the molecular docking protocol (violet = original, cyan = docked)

Table 2 — The interactions between the docked ligands and the protein 4G3F

Docked ligands	Binding energy (kcal/mol)	Hydrogen bond interaction	Van der Waals interaction	Hydrophobic interaction
CPD1	–9.86	Arg410, Glu475, Ser478, Gln481, Asn522, Cys535, Asp536	Gly409, Gly411, Ser412, Arg418, Gly477, Gly480, Asp521	Val408, Arg410, Val416, Ala429, Lys431, Met471, Leu473, Leu474, Leu524, Cys535
CPD2	–9.39	Gly409, Ser478, Lys484, Asp521, Asn522, Cys535, Asp536	Arg410, Gly411, Ser412, Arg418, Leu473, Leu474, Glu475, Gly480, Gln481	Val408, Val416, Ala429, Lys431, Met471, Gly477, Leu524
CPD3	–9.54	Glu442, Leu474, Cys535, Asp536	Gly409, Arg410, Gly411, Ser412, Arg418, Glu475, Gly477, Ser478, Gln481, Asp521, Asn522, Phe537	Val408, Val416, Ala429, Lys431, Leu457, Ile469, Met471, Leu473, Leu524, Cys535, Asp536
CPD4	–7.32	Arg418, Leu474, Glu475, Cys535	Gly409, Arg410, Gly411, Gly477, Ser478, Gln481, Asp521, Asp536	Val408, Val416, Ala429, Lys431, Met471, Leu473, Leu524, Cys535
CPD5	–8.13	Glu472, Cys535	Gly409, Gly411, Arg418, Leu474, Glu475, Gly477, Ser478, Gln481, Asp536	Val408, Val416, Ala429, Lys431, Met471, Leu473, Leu524, Cys535
CPD6	–8.08	Gly411, Arg418, Gln481, Asp521, Asn522	Gly409, Arg410, Ser412, Lys431, Leu473, Leu474, Glu475, Gly477, Ser478, Asp536	Val408, Val416, Ala429, Met471, Leu524, Cys535
CPD7	–8.73	Val408, Arg410, Arg418, Glu475, Gly477, Ser478, Asn522, Cys535, Asp536	Gly409, Gly411, Ser412, Leu474, Gln481, Lys484	Val408, Val416, Ala429, Lys431, Met471, Leu473, Leu524
CPD8	2.19	Val408, Glu475, Gly477, Lys519, Cys535, Asp536	Gly411, Ser412, Arg418, Leu473, Leu474, Ser478, Gln481, Val523	Arg407, Val408, Gly409, Val416, Ala429, Lys431, Met471, Lys484, Asp521, Leu524, CYs535
CPD9	–6.21	Glu475, Asn522, Cys535	Gly409, Arg410, Gly411, Arg418, Leu474, Gly477, Ser478, Gln481, Asp521, Asp536	Val408, Val416, Ala429, Met471, Leu473, Leu524, Cys535
IMD 0354	–7.61	Gly409, Arg410, Ser478, Gln481, Cys535, Asp536	Gly411, Ser412, Ala429, Val430, Glu442, Asn522	Val408, Gly409, Arg410, Val416, Lys431, Ile469, Met471, Gly477, Gln481, Asp521, Leu524, Cys535

the ligand-binding domain, were established. Hydrogen bonding, van der Waals and hydrophobic interactions between the protein and the ligands were characterized through molecular docking, with each specific molecular interaction involving the amino acids of 4G3F illustrated in Fig. 7.

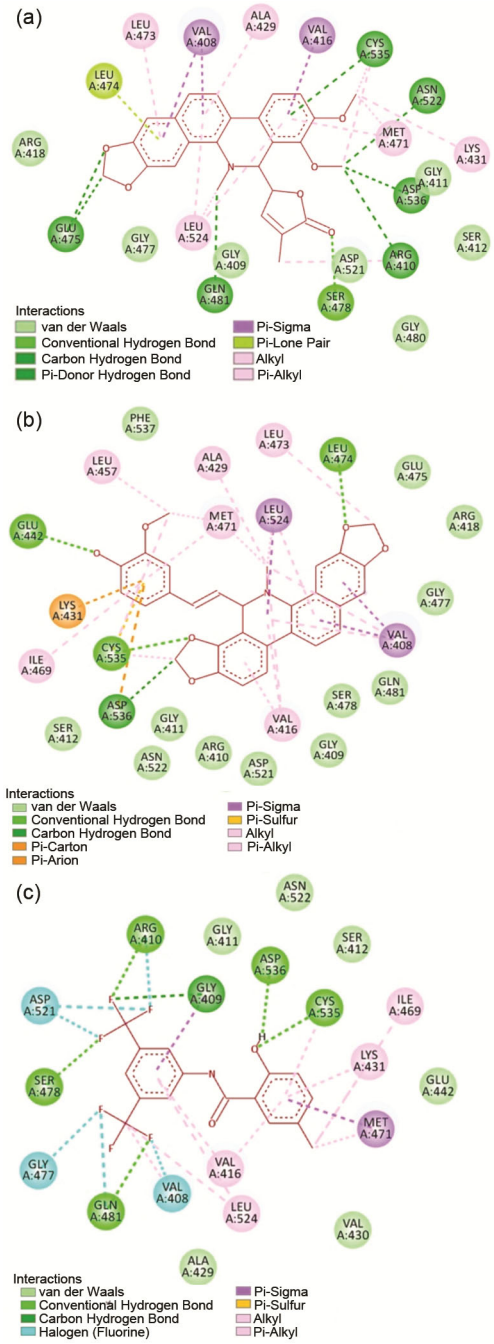

Fig. 7 — 2D interaction diagram between the 4G3F protein receptor and ligands. (A) CPD1, (B) CPD3, and (C) IMD 0354

Docking simulations of the selected alkaloids in association with the 4G3F protein revealed a variety of interaction modalities, including hydrogen bonds, van der Waals forces, and hydrophobic interactions, which collectively enhance the structural stability of the ligand-protein complex. Hydrogen bonds represent specific, energetically favorable interactions involving the sharing of a hydrogen atom between electronegative atoms such as oxygen or nitrogen. Hydrophobic interactions arise from the tendency of nonpolar molecules to aggregate in an aqueous environment, minimizing solvent contact and promoting their association. Although hydrogen bonds exhibit greater strength and directionality, hydrophobic interactions exert a significant influence, particularly in stabilizing extensive protein structures and ligand-binding interfaces[27]. Van der Waals forces play an essential role in stabilizing protein-ligand complexes during molecular docking, contributing to the precise spatial alignment between interacting molecules and augmenting binding affinity in conjunction with hydrogen bonding and hydrophobic effects[28]. These weak, noncovalent interactions are vital for achieving an optimal docking conformation. It is noted that a more negative binding energy indicates a more stable and favorable binding event, suggesting a higher likelihood of ligand retention within the receptor[29].

The selected alkaloids, notably CPD1 and CPD3, demonstrated superior interaction profiles with the 4G3F protein, a key kinase regulating NF-κB signaling in cancer cells. Specifically, CPD1 established a total of 22 interactions, with 13 targeting active sites (Val408, Gly411, Val416, Ala429, Lys431, Glu442, Ile469, Met471, Leu473, Leu474, Asp521, Asn522, Leu534, Asp536), including hydrogen bonds (Arg410, Glu475, Ser478, Gln481, Asn522, Cys535, Asp536) alongside van der Waals interactions (Gly409, Gly411, Ser412, Arg418, Gly477, Gly480, Asp521) and hydrophobic interactions (Val408, Arg410, Val416, Ala429, Lys431, Met471, Leu473, Leu474, Leu524, Cys535). The binding energy of CPD1 with 4G3F reached –9.86 kcal/mol (Fig. 7A), reflecting a highly stable ligand-protein complex. Similarly, CPD3 formed a total of 25 interactions, with 14 engaging key active sites (Val408, Gly411, Val416, Ala429, Glu442, Ile469, Met471, Leu473, Leu474, Asp521, Asn522, Leu524, Asp536), including hydrogen bonds (Glu442, Leu474, Cys535, Asp536) along with van der Waals interactions (Gly409, Arg410, Gly411, Ser412, Arg418, Glu475, Gly477, Ser478, Gln481, Asp521, Asn522, Phe537) and hydrophobic interactions (Val408, Val416, Ala429, Lys431, Leu457, Ile469, Met471, Leu473, Leu524, Cys535, Asp536). The binding energy of CPD3 with 4G3F was –9.54 kcal/mol (Fig. 7C), indicative of significant stability.

In comparison, IMD 0354, utilized as a reference inhibitor, established 20 total interactions, with 11 targeting key active sites including Val408, Gly411, Val416, Ala429, Lys431, Met471, Leu473, Leu474, Asp521, Asn522, Leu524, facilitated by hydrogen bonds (Gly409, Arg410, Ser478, Gln481, Cys535, Asp536) alongside van der Waals interactions (Gly411, Ser412, Ala429, Val430, Glu442, Asn522) and hydrophobic interactions (Val408, Gly409, Arg410, Val416, Lys431, Ile469, Met471, Gly477, Gln481, Asp521, Leu524, Cys535). The binding energy of IMD 0354 with 4G3F was –7.61 kcal/mol (Fig. 7J). Although IMD 0354 exhibited a degree of stability, its less negative binding energy and reduced number of interactions and active site engagements suggest a comparatively less effective interaction profile compared to CPD1 and CPD3.

These findings demonstrate that CPD1 and CPD3, characterized by more negative binding energies (–9.86 kcal/mol and –9.54 kcal/mol) and a greater number of interactions (22 and 25 total, with 13 and 14 at active sites), exhibit enhanced potential to inhibit 4G3F compared to IMD 0354 (–7.61 kcal/mol, 20 interactions, 11 at active sites). The active sites Val408, Gly411, and Leu524, where CPD1 and CPD3 establish robust interactions, play a critical role in modulating the kinase activity of NIK, as supported by structural data indicating their location within the ATP-binding pocket and hydrophobic pocket of the 4G3F structure[13]. These interactions likely disrupt the phosphorylation of IKKα and the processing of p100 into p52, key steps in the non-canonical NF-κB pathway, thereby facilitating effective suppression of NF-κB signaling in gastric cancer cells. The observed disparity between Val408 in murine NIK and the corresponding Leu406 in human NIK, as noted in the structural analysis, warrants further investigation to ensure translational relevance. Consequently, CPD1 and CPD3 emerge as prime candidates for subsequent molecular dynamics simulations, with IMD 0354 serving as a reference inhibitor to further assess the stability and dynamic behavior of the ligand-protein complex within the NIK binding pocket, particularly at these critical active sites.

Molecular dynamics simulation

Molecular dynamics simulations offer a detailed understanding of the temporal evolution and stability of the protein-ligand complex, elucidating conformational alterations and structural integrity[30]. This technique is performed after molecular docking to validate and refine the results obtained from docking studies. The analysis comprehensively evaluated the RMSD, RMSF, Rg, H-bond, and SASA results to assess the stability, flexibility, and solvent accessibility of the CPD1-4G3F, CPD3-4G3F and IMD 0354-4G3F complexes over the simulation trajectory. As a result, the total energy was calculated as –467,444 kJ/mol for CPD1-4G3F complex and –467,499 kJ/mol for CPD3-4G3F complex. The potential values were calculated as –584,987 kJ/mol for CPD1-4G3F complex and –585,016 kJ/mol for CPD3-4G3F complex. The total energy and potential values of IMD 0354-4G3F complex were calculated as –467,645 kJ/mol and –585,107 kJ/mol, respectively. The system was equilibrated at a temperature of 300 K.

In molecular dynamics simulations, the root-mean-square deviation (RMSD) serves as a vital parameter for evaluating the structural resemblance between two molecular conformations, typically following optimal alignment of their frameworks. This metric quantifies the average displacement between corresponding atoms across the two structures, with lower RMSD values signifying greater structural similarity[31]. The RMSD values for the CPD1-4G3F and CPD3-4G3F complexes, recorded over a 100 ns simulation period, ranged from approximately 0.15 to 0.36 nm (Fig. 8A). These findings suggest that the CPD1-4G3F complex maintained highly stable structural deviations, with RMSD values consistently confined between 0.20 and 0.25 nm, reflecting a robust binding interaction with the 4G3F protein. Similarly, the CPD3-4G3F complex exhibited RMSD values spanning 0.15 to 0.25 nm, indicating exceptional structural stability and a strong binding affinity with 4G3F. In contrast, the IMD 0354-4G3F complex displayed RMSD values ranging from 0.15 to 0.29 nm, demonstrating slightly greater structural variability while remaining within an acceptable range. This disparity suggests that CPD1 and CPD3 may establish more secure binding affinities with 4G3F compared to IMD 0354, thereby enhancing structural stability within the binding pocket. Consequently, it can be concluded that CPD1 and CPD3 preserve their initial configurations more effectively than IMD 0354, as substantiated by the current dynamic evaluation.

The root-mean-square fluctuation (RMSF) serves as a key metric in molecular dynamics simulations to assess the average displacement of each residue's

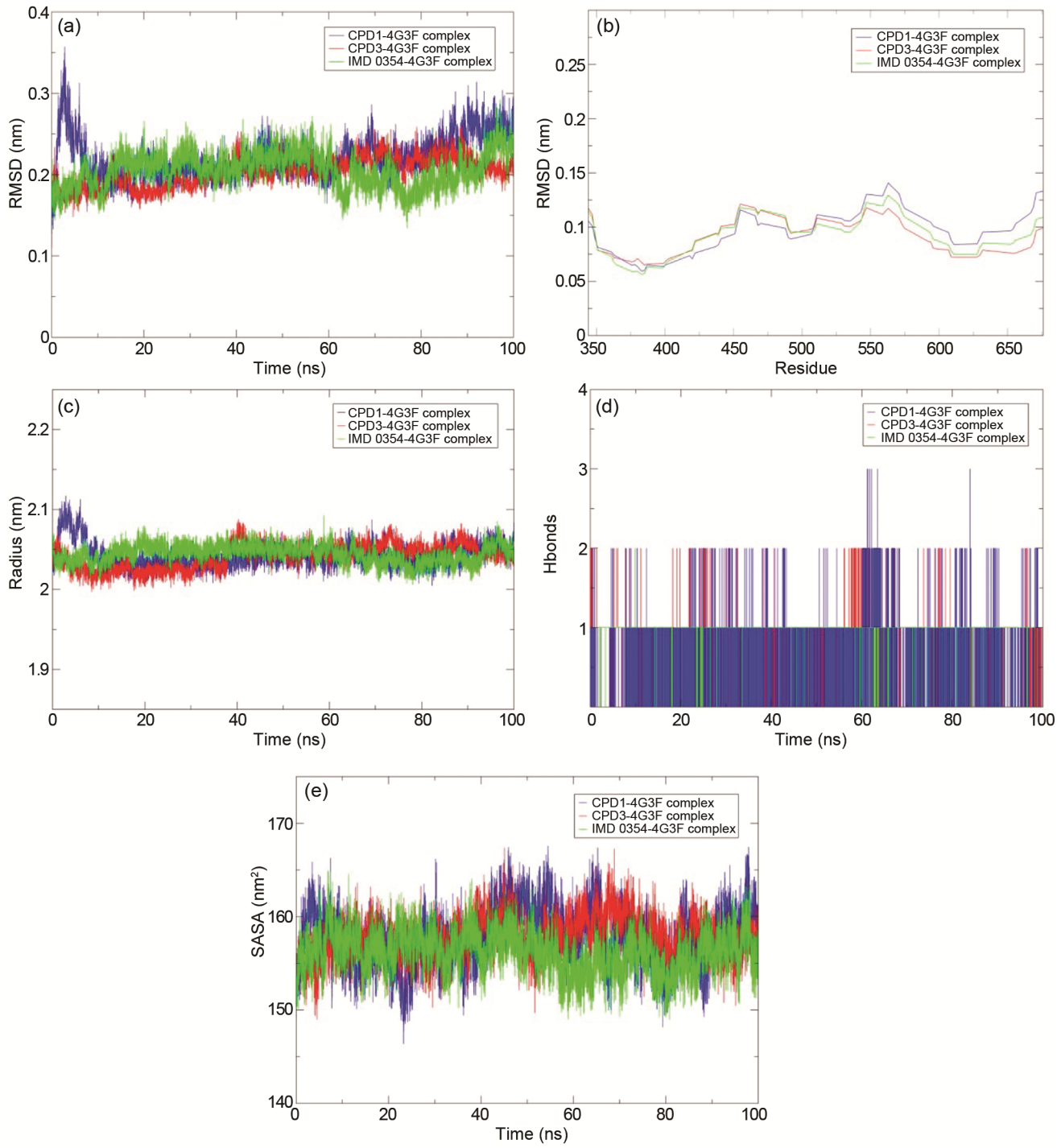

Fig. 8 — Molecular dynamics simulation results for the bindings of CPD1 (blue), CPD3 (red) and IMD 0354 (green) with 4G3F protein. (A) RMSD, (B) RMSF, (C) Rg, (D) H-bonds, and (E) SASA

position relative to a reference structure over the simulation duration, thereby reflecting its degree of flexibility or mobility[32]. Fig. 8B presents the RMSF values for the CPD1-4G3F, CPD3-4G3F, and IMD 0354-4G3F complexes, recorded over a 100 ns simulation period, exhibiting a consistent range of flexibility across residues Ser344 to Gly676, encompassing the entire polypeptide chain of the 4G3F protein. This variability may correlate with the spatial arrangement of these residues relative to the

primary active binding sites, which include significant residues such as Val408, Gly411, and Leu524. Notably, the IMD 0354-4G3F complex displayed elevated RMSF values at specific segments, particularly residues approximately 450 to 550, indicating increased mobility in these regions compared to the CPD1-4G3F and CPD3-4G3F complexes. This observation suggests that IMD 0354 may experience more pronounced conformational changes, potentially affecting the stability of its association within the 4G3F binding pocket. Consequently, it can be inferred that the CPD1-4G3F and CPD3-4G3F complexes sustain a more stable conformation with reduced flexibility, highlighting the potential of CPD1 and CPD3 to effectively regulate biological interactions within the 4G3F protein.

The radius of gyration (Rg) quantifies the compactness of a protein by computing the root mean square distance of each atom from the protein's center of mass, thereby providing an indicator of the spatial distribution of its structure[33]. A reduced Rg value signifies a more condensed configuration, whereas an elevated Rg value denotes a more extended arrangement. The evaluation of Rg values for each complex is presented in Fig. 8C. The Rg values for the CPD1-4G3F, CPD3-4G3F, and IMD 0354-4G3F complexes exhibited consistent stability around 2.05 nm, confirming all complexes maintain a relatively compact structure of the 4G3F protein throughout the simulation period.

Hydrogen bonds play an important role in molecular dynamics simulations, substantially affecting the structural stability, conformational dynamics, and intermolecular interactions of molecules[34]. Hydrogen bonds were consistently present throughout the simulation period, with the CPD1-4G3F complex sustaining between 1 and 3 bonds, the CPD3-4G3F complex maintaining between 1 and 2 bonds, and the IMD 0354-4G3F complex exhibiting between 1 and 2 bonds. These observations indicate that all complexes remained stably associated within the 4G3F protein binding pocket throughout the simulation duration, with the CPD1-4G3F complex demonstrating a notably higher number of hydrogen bonds compared to the CPD3-4G3F and IMD 0354-4G3F complexes (Fig. 8D). This difference suggests that CPD1 establishes a more pronounced bonding interaction with the 4G3F protein.

The solvent-accessible surface area (SASA) quantifies the extent of a molecule's surface exposed to solvent molecules, serving as a critical parameter for elucidating molecular interactions and conformational transitions, thereby offering insights into protein folding, stability, and biomolecular associations[35]. The SASA values were assessed to examine the solvent exposure of the CPD1-4G3F, CPD3-4G3F, and IMD 0354-4G3F complexes. The SASA plot revealed dynamic fluctuations over the 100 ns simulation period, with all complexes displaying variations ranging from 150 to 165 nm², resulting in an average value of approximately 157 nm² (Fig. 8E). These variations indicate ligand-induced structural modifications in solvent accessibility, suggesting adjustments at the 4G3F -ligand interface that may impact binding properties. The uniformity in the fluctuation range and comparable average values across the three complexes reflects a consistent maintenance of the solvent-exposed surface, notwithstanding the notably more negative docking binding energies of CPD1 (–9.86 kcal/mol) and CPD3 (–9.54 kcal/mol) compared to IMD 0354 (–7.61 kcal/mol), implying potential distinctions in binding dynamics.

The comprehensive evaluation of dynamic parameters has delivered an in-depth understanding of the stability and structural properties of the CPD1-4G3F, CPD3-4G3F, and IMD 0354-4G3F complexes, underscoring the role of the 4G3F protein in facilitating biological interactions. The analysis indicated that the CPD1-4G3F and CPD3-4G3F complexes manifest greater stability relative to the IMD 0354-4G3F complex's association with the 4G3F protein, positioning CPD1 and CPD3 as prospective candidates. These findings, consistent with the more negative docking binding energies of CPD1 (–9.86 kcal/mol) and CPD3 (–9.54 kcal/mol) compared to IMD 0354 (–7.61 kcal/mol), highlight their ability to sustain effective binding with the 4G3F protein.

Drug likeness and ADMET prediction

In pharmaceutical research, a chemical compound must exhibit favorable physicochemical attributes, appropriate pharmacokinetic profiles, and desired pharmacological efficacy to qualify as a viable drug candidate. These characteristics are essential for ensuring the compound's effectiveness, safety, and suitability for progression into drug development.

Recent advancements in computer-assisted estimations of ADMET (absorption, distribution, metabolism, excretion, and toxicity) properties within drug discovery have substantially diminished the time, cost, and resource investment required for drug development by facilitating the early identification and exclusion of less promising candidates[36]. Consequently, ADMET predictions were performed utilizing the pkCSM database to evaluate the oral bioavailability of CPD1 and CPD3 in comparison to IMD 0354[19], with comprehensive results presented in Table 3.

Drug absorption constitutes the process by which a pharmaceutical agent translocates from its site of administration into the systemic circulation, representing the initial phase of pharmacokinetics, which delineates the body's handling of a drug. In the context of drug absorption, a value below 30% often indicates poor bioavailability[37]. Within the present investigation, CPD1 demonstrated an absorption rate of 100%, while CPD3 exhibited 99.257%, both markedly exceeding the threshold for low absorption and indicating favorable gastrointestinal bioavailability. In comparison, IMD 0354 recorded an absorption rate of 82.653%, which, while substantial, remains lower than that of CPD1 and CPD3. The water solubility values, with CPD1 at –4.235 log mol/L, CPD3 at –3.313 log mol/L, and IMD 0354 at –6.028 log mol/L, suggest that CPD3 possesses the highest solubility, potentially enhancing its absorption efficiency, whereas IMD 0354 exhibits the lowest solubility, which may impede its bioavailability. However, CPD1 and CPD3 compensate with higher Caco2 permeability values of 1.52 and 1.048 log Papp in 10^{-6} cm/s, respectively, compared to 1.478 log Papp in 10^{-6} cm/s for IMD 0354, indicating superior

Table 3 — Predicted ADMET properties of CPD1, CPD3 and IMD 0354

ADMET properties	Unit	CPD1	CPD3	IMD 0354
Water Solubility	(Log mol/L)	–4.235	–3.313	–6.028
Caco2 permeability	(Log Papp in 10^{-6} cm/s)	1.52	1.048	1.478
Intestinal absorption (Human)	(% Absorbed)	100	99.257	82.653
Skin permeability	(Log Kp)	–2.735	–2.735	–2.899
P-glycoprotein substrate	Yes/No	No	Yes	Yes
P-glycoprotein I inhibitor	Yes/No	Yes	Yes	Yes
P-glycoprotein II inhibitor	Yes/No	Yes	Yes	No
VDss	(Log L/kg)	–0.826	–1.577	–0.225
Fraction unbound (human)	(Fu)	0.192	0.353	0
BBB permeability	(Log BB)	–0.522	–0.702	0.099
CNS permeability	(Log PS)	–3.15	–2.847	–1.574
CYP2D6 substrate	Yes/No	No	No	No
CYP3A4 substrate	Yes/No	Yes	Yes	Yes
CYP1A2 inhibitor	Yes/No	No	No	Yes
CYP2C19 inhibitor	Yes/No	Yes	Yes	Yes
CYP2C9 inhibitor	Yes/No	Yes	Yes	Yes
CYP2D6 inhibitor	Yes/No	No	No	No
CYP3A4 inhibitor	Yes/No	No	No	No
Total clearance	(Log mL/min/kg)	0.54	0.133	0.012
Renal OCT2 substrate	Yes/No	No	No	Yes
AMES toxicity	Yes/No	No	Yes	No
Max. tolerated dose (human)	(Log mg/kg/day)	0.325	0.43	0.45
hERG I inhibitor	Yes/No	No	No	No
hERG II inhibitor	Yes/No	Yes	Yes	No
Oral rat acute toxicity (LD50)	(mol/kg)	3.15	2.818	2.472
Oral rat chronic toxicity (LOAEL)	(Log mg/kg_bw/day)	1.024	0.602	1.636
Hepatotoxicity	Yes/No	No	Yes	No
Skin sensation	Yes/No	No	No	No
Tetrahymena pyriformis toxicity	(Log ug/L)	0.285	0.285	1.525
Minnow toxicity	(Log mM)	–2.87	–2.823	0.805

membrane permeability. Concerning P-glycoprotein interactions, CPD1 is neither a substrate nor an inhibitor, potentially reducing efflux effects and enhancing bioavailability. CPD3 acts as a P-glycoprotein substrate but inhibits both I and II isoforms, whereas IMD 0354 serves as a substrate and inhibits only P-glycoprotein I, suggesting that CPD1 may experience fewer efflux-related limitations, while CPD3 and IMD 0354 could face increased risks of drug resistance *in vivo* due to such mechanisms.

In ADMET prediction, distribution indicates the mechanism by which a pharmaceutical agent disperses from the bloodstream to diverse tissues and organs throughout the body, reflecting its dissemination following absorption into systemic circulation. Key distribution parameters include the volume of distribution at steady state (VDss), where a value exceeding 0.45 log L/kg indicates extensive distribution[38]. The distribution profiles for CPD1, CPD3, and IMD 0354 revealed distinct patterns, with CPD1 exhibiting a VDss of –0.826 log L/kg, CPD3 at –1.577 log L/kg, and IMD 0354 at –0.225 log L/kg, suggesting a limited distribution volume for all three, with CPD3 demonstrating the most restricted dispersion. For blood-brain barrier (BBB) permeability, a log BB value greater than 0.3 denotes favorable penetration, whereas values below –1 signify poor permeability[39]; CPD1 with a log BB of –0.522, CPD3 with –0.702, and IMD 0354 with 0.099 indicate poor to moderate BBB penetration, with IMD 0354 showing the least restriction in crossing this barrier. Regarding central nervous system (CNS) permeability, compounds with log PS values exceeding –2 exhibit CNS penetration capability, while those with log PS below –3 lack such potential[40]. CPD1 with a log PS of –3.15, CPD3 with –2.847, and IMD 0354 with –1.574 fall into the poor to moderate penetration category, with CPD1 demonstrating the lowest CNS accessibility. The fraction unbound (Fu) values, with CPD1 at 0.192, CPD3 at 0.353, and IMD 0354 at 0, reflect varying degrees of protein binding, where CPD3's higher unbound fraction suggests enhanced availability for distribution, potentially augmenting its efficacy, whereas the complete protein binding of IMD 0354 may constrain its free distribution *in vivo*, increasing the likelihood of diminished bioavailability.

The prediction of metabolism constitutes an important aspect of drug discovery, as it influences a drug's efficacy and safety profile. Comprehension of a drug's metabolic fate facilitates the determination of its duration of action, potential for drug-drug interactions, and susceptibility to toxicity. Cytochrome P450 (CYP450) enzymes represent a substantial and significant enzyme family predominantly involved in the metabolism of pharmaceuticals and other xenobiotics, as well as endogenous compounds such as hormones and lipids. These enzymes fulfill essential functions in detoxification, cellular metabolism, and the maintenance of homeostasis, with their primary localization in the liver and additional presence in tissues such as the intestines and kidneys. The human genome encompasses 18 mammalian CYP families, encoding a total of 57 genes, with the CYP1, CYP2, CYP3, and CYP4 families exhibiting prominent representation and containing a substantial number of genes, particularly CYP2, CYP3, and CYP4[41,42]. Among these, CYP1A2, CYP2C9, CYP2C19, CYP2D6, and CYP3A4 emerge as primary enzymes responsible for metabolizing the majority of drugs during the initial phase of metabolism[43]. The metabolic profiles of CPD1, CPD3, and IMD 0354 reveal distinct characteristics that affect their pharmacokinetics and potential drug interactions. CPD1 and CPD3 function as substrates for CYP3A4 but exhibit no substrate activity for CYP2D6, while CPD1 inhibits CYP2C19 and CYP2C9, and CPD3 inhibits CYP2C19 and CYP2C9, with neither inhibiting CYP1A2, CYP2D6, or CYP3A4. In contrast, IMD 0354 serves as a CYP3A4 substrate and inhibits CYP1A2, CYP2C19, and CYP2C9, but not CYP2D6 or CYP3A4. These profiles indicate a predominant reliance on CYP3A4 metabolism for all three compounds, with CPD1 and CPD3 demonstrating a selective inhibitory pattern that may reduce the risk of extensive drug-drug interactions, whereas IMD 0354's broader inhibition profile suggests a higher potential for such interactions. These metabolic characteristics imply that CPD1 and CPD3 maintain stable pharmacokinetics with a potentially lower interaction liability, while IMD 0354 requires careful consideration of CYP-mediated interactions to optimize therapeutic efficacy in anticancer applications.

Drug excretion entails the elimination of a pharmaceutical agent through pathways such as urinary and biliary routes, with kidneys and liver as primary organs, influencing drug half-life and dosing frequency. The excretion properties of CPD1, CPD3,

and IMD 0354 were evaluated, revealing total clearance rates of 0.54, 0.133, and 0.012 log mL/min/kg, respectively, indicating rapid clearance for CPD1, moderate for CPD3, and minimal for IMD 0354. Neither CPD1 nor CPD3 serves as a renal OCT2 substrate, unlike IMD 0354, suggesting prolonged systemic presence for IMD 0354, potentially reducing dosing frequency. The higher clearance of CPD1 and CPD3 may necessitate frequent administration, yet their docking binding affinities (–9.86 kcal/mol and –9.54 kcal/mol) support effective target engagement, whereas IMD 0354's lower clearance (0.012 log mL/min/kg) and less negative binding energy (–7.61 kcal/mol) may enhance persistence but limit efficacy in gastric cancer therapy.

ADMET analyses, with a particular emphasis on toxicity, are essential for delivering safe and efficacious pharmaceuticals to patients, serving as a critical filter in the drug development process to identify and exclude compounds exhibiting unfavorable toxicity profiles prior to clinical trials. The Ames test represents a widely adopted method for evaluating the mutagenic potential of a substance, offering a rapid and cost-effective approach to screen chemicals for possible carcinogenic effects, thereby complementing traditional, resource-intensive animal-based carcinogenicity assessments[44]. The toxicity properties were assessed to establish the safety profile of CPD1, CPD3, and IMD 0354 for potential therapeutic use. CPD3 displayed AMES toxicity, indicating potential mutagenic effects, whereas CPD1 and IMD 0354 exhibited no AMES toxicity, suggesting a more favorable genetic safety profile. The maximum tolerated dose values were 0.325 log mg/kg/day for CPD1, 0.43 log mg/kg/day for CPD3, and 0.45 log mg/kg/day for IMD 0354, implying a slightly higher dose tolerance for IMD 0354. None of the compounds demonstrated hepatotoxicity, skin sensitization, or inhibition of hERG I, though CPD1 and CPD3 exhibited hERG II inhibition, while IMD 0354 did not, indicating a reduced cardiac toxicity risk for IMD 0354. Oral rat acute toxicity (LD50) values were 3.15 mol/kg for CPD1, 2.818 mol/kg for CPD3, and 2.472 mol/kg for IMD 0354, reflecting comparable lethal dose thresholds. Chronic toxicity (LOAEL) was 1.024 log mg/kg_bw/day for CPD1, 0.602 log mg/kg_bw/day for CPD3, and 1.636 log mg/kg_bw/day for IMD 0354, suggesting a lower chronic exposure risk for CPD3. *Tetrahymena pyriformis* toxicity was 0.285 log ug/L for both CPD1 and CPD3, compared to 1.525 log ug/L for IMD 0354, while minnow toxicity was –2.87 log mM for CPD1, –2.823 log mM for CPD3, and 0.805 log mM for IMD 0354, indicating a mixed environmental toxicity profile with lower aquatic toxicity for CPD1 and CPD3. Collectively, the safety data, in conjunction with the stable binding affinities of CPD1 (–9.86 kcal/mol) and CPD3 (–9.54 kcal/mol) to 4G3F, support their potential as anticancer agents for gastric cancer therapy. Nevertheless, additional *in vivo* investigations are recommended to validate these findings and address the mutagenic concerns associated with CPD3.

Based on the *in silico* ADMET evaluation outcomes for CPD1 and IMD 0354, it can be inferred that CPD1 presents a promising pharmacokinetic profile, characterized by excellent absorption, limited distribution, stable metabolism *via* CYP3A4, and a balanced clearance rate. With no AMES toxicity detected, CPD1's enhanced stability and favorable binding affinity to 4G3F (–9.86 kcal/mol) highlight its potential as a lead compound for anticancer therapy, particularly in targeting gastric cancer through NF-κB inhibition. Furthermore, CPD1 may serve as a foundation for developing novel compounds with optimized safety profiles, improved biological activities, and innovative therapeutic applications focused on modulating NF-κB signaling, while IMD 0354, despite its favorable profile, exhibits a lower binding affinity (–7.61 kcal/mol) and warrants further safety assessment due to its broader CYP inhibition.

Conclusions

In conclusion, the investigation effectively implemented network pharmacology, molecular docking, and molecular dynamics simulations for alkaloids derived from Macleaya microcarpa, recognized for their potential to interact with the 4G3F protein (NIK kinase). The network pharmacology approach established an initial framework for identifying potential biological targets, while molecular docking results demonstrated that CPD1 exhibits superior stability and precise positioning within the 4G3F binding pocket compared to IMD 0354. The molecular dynamics simulation outcomes over a 100 ns period elucidated a sustained interaction mechanism, with stable binding associations between CPD1 and 4G3F, confirming a consistent and robust engagement with this kinase.

These findings validate the capacity of CPD1 to maintain effective associations with 4G3F throughout the simulation duration, underscoring its prominence as a potential NIK inhibitor for targeting gastric cancer through modulation of the NF-κB pathway.

Nevertheless, while computational predictions identify promising candidates, it remains essential to emphasize the necessity of experimental validation to confirm the reliability of these results. Due to the absence of available equipment resources, the present study did not include experimental assessments. However, future research is recommended to prioritize *in vitro* and *in vivo* experiments to comprehensively evaluate the interaction properties of CPD1. Such experiments should assess the compound's effects on biological models, thereby determining its efficacy and safety profile. The lack of *in vitro* and *in vivo* data, coupled with the absence of an evaluation for unintended covalent inhibition, represents limitations of this investigation. Should CPD1 demonstrate potential in preclinical studies, it may warrant prioritization for subsequent clinical evaluations. Although further research is required to deepen understanding, the findings of this study establish a robust foundation for future explorations and provide a promising direction for advancing therapeutic applications.

Supplementary Information

Supplementary information is available in the website https://nopr.niscpr.res.in/handle/123456789/58776.

Funding

No funding was received for conducting this research.

Conflict of Interest

The authors declare that there are no conflicts of interest.

Author's Contributions

The authors confirms the sole responsibility for the conception of the study, presented results and manuscript preparation. All data were generated in-house and that no paper mill was used.

References

1 Bray F, Laversanne M, Sung H, Ferlay J, Siegel R L, Soerjomataram I & Jemal A, *CA Cancer J Clin*, 74 (2024) 229.
2 Guan W L, He Y & Xu R H, *J Hematol Oncol*, 16 (2023) 57.
3 Qi F, Zhao L, Zhou A, Zhang B, Li A, Wang Z & Han J, *Biosci Trends*, 9 (2015) 16.
4 Xiang Y, Guo Z, Zhu P, Chen J & Huang Y, *Cancer Med*, 8 (2019) 1958.
5 Wang K, Chen Q, Shao Y, Yin S, Liu C, Liu Y, Wang R, Wang T, Qiu Y & Yu H, *Biomed Pharmacother*, 133 (2021) 111044.
6 Koochaki R, Amini E, Zarehossini S, Zareh D, Haftcheshmeh S M, Jha S K, Kesharwani P, Shakeri A & Sahebkar A, *Fitoterapia*, 179 (2024) 106222.
7 Zhang T, Ma C, Zhang Z, Zhang H & Hu H, *MedComm*, 2 (2021) 618.
8 Deng A & Qin H, *Phytochemistry*, 71 (2010) 816.
9 Keiser M J, Roth B L, Armbruster B N, Ernsberger P, Irwin J J & Shoichet B K, *Nat Biotechnol*, 25 (2007) 197.
10 Szklarczyk D, Gable A L, Nastou K C, Lyon D, Kirsch R, Pyysalo S, Doncheva N T, Legeay M, Fang T, Bork P, Jensen L J & von Mering C, *Nucleic Acids Res*, 49 (2021) D605.
11 Clarke D J B, Kuleshov M V, Schilder B M, Torre D, Duffy M E, Keenan A B, *Nucleic Acids Res*, 46 (2018) W171.
12 Nguyen H D, *Indian J Chem*, 64 (2025) 383.
13 de Leon-Boenig G, Bowman K K, Feng J A, Crawford T, Everett C, Franke Y, Oh A, Stanley M, Staben S T, Starovasnik M A, Wallweber H J A, Wu J, Wu L C, Johnson A R & Hymowitz S G, *Structure*, 20 (2012) 1704.
14 Laskowski R A, MacArthur M W, Moss D S & Thornton J M, *J Appl Crystallogr*, 26 (1993) 283.
15 Van Der Spoel D, Lindahl E, Hess B, Groenhof G, Mark A E & Berendsen H J C, *J Comput Chem*, 26 (2005) 1701.
16 Guex N & Peitsch M C, *Electrophoresis*, 18 (1997) 2714.
17 Zoete V, Cuendet M A, Grosdidier A & Michielin O, *J Comput Chem*, 32 (2011) 2359.
18 Pettersen E F, Goddard T D, Huang C C, Couch G S, Greenblatt D M, Meng E C & Ferrin T E, *J Comput Chem*, 25 (2004) 1605.
19 Pires D E, Blundell T L & Ascher D B, *J Med Chem*, 58 (2015) 4066.
20 Morrison H A, Eden K, Trusiano B, Rothschild D E, Qin Y, Wade P A, Rowe A J, Mounzer C, Stephens M C, Hanson K M, Brown S L, Holl E K & Allen I C, *Cell Mol Gastroenterol Hepatol*, 18 (2024) 101356.
21 Noort A R, van Zoest K P M, Weijers E M, Koolwijk P, Maracle C X, Novack D V, Siemerink M J, Schlingemann R O, Tak P P & Tas S W, *J Pathol*, 234 (2014) 375.
22 Philip S, Sherin D R, Kumar T K M, Badisha Banu T C & Roy R M, *Mol Divers*, 28 (2024) 1459.
23 Chen J & Stark L A, *Trends Genet*, 35 (2019) 768.
24 Thoms H C & Stark L A, The NF-κB Nucleolar Stress Response Pathway, *Biomedicines*, 9 (2021) 1082.
25 Nitiss J L, *Nat Rev Cancer*, 9 (2009) 338.
26 Ramírez D & Caballero J, *Molecules*, 23 (2018) 1038.
27 Chen D, Oezguen N, Urvil P, Ferguson C, Dann S M & Savidge T C, *Sci Adv*, 2 (2025) e1501240.
28 Yao W, Mo L, Fang L & Qin L, *Ecotoxicol Environ Saf*, 256 (2023) 114910.
29 Bitencourt-Ferreira G, Veit-Acosta M & De Azevedo W F, *Van der Waals Potential in Protein Complexes*, (Springer, New York) 2019, p. 79.
30 Hollingsworth S A & Dror R O, *Neuron*, 99 (2018) 1129.

31 Prabantu V M, Gadiyaram V, Vishveshwara S & Srinivasan N, *Curr Res Struct Biol*, 4 (2022) 134.

32 Bufarwa S M, Belaidi M, Abbass L M & Thbayh D K, *Appl Organomet Chem*, 39 (2025) e7953.

33 Victorien Hermann H D, Jules F J & Jeanet C, *Discov Appl Sci*, 7 (2025) 749.

34 Khan A, Waheed Y, Kuttikrishnan S, Prabhu K S, El-Elimat T, Uddin S, Alali F Q & Agouni A, *Front Pharmacol*, 15 (2024) 1352907.

35 Bogatyreva N S & Ivankov D N, *Mol Biol*, 42 (2008) 932.

36 Bunally S B, Luscombe C N & Young R J, *Slas Discov*, 24 (2019) 791.

37 Stielow M, Witczyńska A, Kubryń N, Fijałkowski Ł, Nowaczyk J & Nowaczyk A, *Molecules*, 28 (2023) 8038.

38 Ibrahim M, Detroja A, Bhimani A, Bhatt T C, Koradiya J, Sanghvi G & Bishoyi A K, *Heliyon*, 11 (2025) e42859.

39 Usansky H H & Sinko P J, *Pharm Res*, 20 (2003) 390.

40 Carpenter T S, Kirshner D A, Lau E Y, Wong S E, Nilmeier J P & Lightstone F C, *Biophys J*, 107 (2014) 630.

41 Zhao M, Ma J, Li M, Zhang Y, Jiang B, Zhao X, Huai C, Shen L, Zhang N, He L & Qin S, *Int J Mol Sci*, 22 (2021) 12808.

42 Nebert D W, Wikvall K & Miller W L, *Philos Trans R Soc B Biol Sci*, 368 (2013) 20120431.

43 Iacopetta D, Ceramella J, Catalano A, Scali E, Scumaci D, Pellegrino M, Aquaro S, Saturnino C & Sinicropi M S, *App Sci*, 13 (2023) 6045.

44 Föllmann W, Degen G, Oesch F & Hengstler J G, *Ames Test*, (Academic Press, San Diego) 2013, p. 104.